Research Papers

Integrated experimental and theoretical study on the phase transition and photoluminescent properties of $ZrO_2:xTb^{3+}$ (x=1, 2, 4 and 8 mol %)

L.X. Lovisa [g,*], Eduardo O. Gomes [b], Lourdes Gracia [c,f], A.A.G. Santiago [a], M. Siu Li [d], Juan Andrés [b,*], E. Longo [e], M.R.D. Bomio [a], F.V. Motta [a]

[a] LSQM – Laboratory of Chemical Synthesis of Materials – Department of Materials Engineering, Federal University of Rio Grande do Norte, P.O. Box 1524, Natal, RN 59078-900, Brazil
[b] Department de Química Física i Analítica, Universitat Jaume I, Castelló de la Plana 12071, Spain
[c] Department of Physical Chemistry, University of Valencia (UV), Burjassot 46100, Spain
[d] IFSC, USP, Av. Trabalhador São Carlense, 400, CEP, São Carlos, SP 13566-590, Brazil
[e] CDMF-LIEC, UFSCar, P.O. Box 676, São Carlos, SP 13565-905, Brazil
[f] Departament de Química Física i Analítica, Universitat Jaume I, 12071, Castelló de la Plana, Spain
[g] Institute of Physics and Chemistry, Federal University of Itajubá (UNIFEI), Itajubá, MG, 37500-903, Brazil

ARTICLE INFO

ABSTRACT

Zirconia (ZrO_2) has been intensively studied as an important ceramic material, and numerous technological applications have been found. The present work deals with synthesizing and characterizing the phase transition (cubic *vs* tetragonal) and photoluminescence emissions of $ZrO_2:xTb^{3+}$ (x = 1,2,4 and 8 mol%). The samples formed by the complex polymerization were thoroughly characterized for physicochemical properties such powder by X-ray diffraction (XRD), and Raman and diffuse reflectance spectroscopies. First-principle calculations at the density functional theory level were performed to complement and rationalize the experimental results. An energy transfer mechanism which promoted the f-f transitions and emitted strong characteristic emissions of Tb^{3+} is discussed in detail. A ZrO_2 lattice acts as an effective sensitizer and the green light emission and the color purity were controlled by the concentration of the Tb^{3+} cations. Moreover, this study enables us to construct a more consistent picture of the doping process of Tb^{3+} in ZrO_2 and provides a new approach for fabricating a multifunctional material and prospective application in lighting devices.

1. Introduction

Materials composed of rare earth (RE^{3+}) cations have recently garnered renewed attention for use in different technological applications [1–4]. Characteristics of RE^{3+} cations are their emission of narrow and well-defined transitions which extend from the visible-infrared range (f → f type transitions), and enable an expressive number of luminescent properties. In particular, the presence of RE^{3+} cations provide superior performance for high-tech applications in optical and communications devices [5–7].

The Eu^{3+} and Tb^{3+} cations are the most studied activators in the RE^{3+} family with intensive emissions located in the visible region due to the fact they are more resistant to the changes provoked by external structural modifications and vibrations, displaying higher luminescence purity and quantum yields [8]. The Tb^{3+} cation has been widely used for

practical applications such as scintillators, phosphors, optical windows and lasers [9–11]. Their luminescent applications are mainly associated to the $^5D_3$ and $^5D_4$ levels of the $4f^8$ configuration of the Tb^{3+} cation [12–15]. These bands usually cover the range from 370 to 680 nm, while the green emissions of Tb^{3+} are mainly located around 550 nm by the $^5D_4 \rightarrow {}^7F_5$ transitions, which is close to the ideal standards required for the green tricolor component [11,16,17].

Zirconia (ZrO_2) is a classic environmentally friendly oxide, presents excellent thermal stability and tunable physicochemical properties [18–21], and its optical properties are strongly affected by the presence of defects [22,23]. ZrO_2 is used as a host matrix of RE^{3+} cations [24] guaranteeing satisfactory energy transfer processes. Crystalline ZrO_2 has a large bandgap (4–6 eV), a high refractive index (2.13–2.20), and a small absorption capacity in the visible and near-infrared spectral regions in combination with low phonon energy (470 cm^{-1}) [25], which

---

* Corresponding authors.
E-mail addresses: lauraengmat@hotmail.com (L.X. Lovisa), andres@qfa.uji.es (J. Andrés).

reduces the probability of the non-radiative multiphonon relaxation of excited RE^{3+} cations [26–28]. ZrO_2 also exhibits two types of electronic transitions: (i) direct at 5.22 eV; and (ii) indirect at 5.87 eV [29]; and high performance in energy conversion [30, 31]. . The band structure is highly dependent on the crystalline structure, the size of crystallites and the nature of the defects [32,33].

ZrO_2 can exist in three distinct phases at ambient pressure: monoclinic, tetragonal, and cubic. The monoclinic phase is thermodynamically stable at ambient temperatures, whereas tetragonal and cubic polymorphs can be obtained by heat treatment at high temperatures [34, 35], the inclusion of dopant metals with a lower valence into the crystal lattice, and also by increasing the surface energy of nanoparticles [36–39]. The use of dopants [23,40,41] favors stabilizing the cubic and tetragonal phases at room temperature. In addition, changes in the crystal structure and then the morphology of ZrO_2 can also lead to modifications in the excitation and emission spectra. Thus, this subtle difference makes studying phase transition very important. In this context, there is still a lot of space for studies dedicated to understanding the relationship between the luminescence properties of the ZrO_2 systems doped with RE^{3+} cations. Our research groups recently presented a combined experimental and theoretical study on the photoluminescence (PL) properties of ZrO_2:Tm^{3+}, Tb^{3+}, Eu^{3+} powders [24]. Tiwari et al [42] evaluated the change effect in Eu^{3+} concentration on structural, photo, and thermoluminescent properties. Colbea et al. [43] disclosed the relationship between the doping concentration of Eu^{3+} and phase transformation of ZrO_2. Very recently, Liu et al. [44] analyzed the PL properties of Eu^{3+} doped ZrO_2 with different morphologies and crystal structures. Vidya et al [45] investigated the color-adjustable photocatalytic activity and PL emissions, and phase transformation of ZrO_2: Tb^{3+} particles. Hui et al. [46], Marin et al. [47], Ahemen and Dejene [48] and Colbea et al. [43] have disclosed the relationship between the doping concentration of Eu^{3+} and phase transformation of ZrO_2. Furthermore, the influence of calcinating ZrO_2:Tb^{3+} powders on the PL properties was examined by Marí et al. [49]. Das et al. [50] recently studied the synthesis, and structural and PL characterization of ZrO_2: Dy^{3+}-Eu^{3+} as promising material with tunable white light [51].

It is well known that the controllable phase of crystals plays a crucial role in order to meet the optical requirements of the above applications, including the intensity, color and luminescence decay time. In this work, we systematically explore the role of Tb^{3+} as a luminescence enhancer in ZrO_2:Tb^{3+}(x = 1,2,4 and 8 mol%) material. The samples were prepared by the complex polymerization (CP) method and characterized by XRD, and Raman and diffuse reflectance spectroscopies. The relationship among the amount of Tb^{3+} in the ZrO_2 host lattice, PL emissions, and phase composition (cubic *vs* tetragonal) were analyzed in detail for the first time. Changes in the Raman vibrational frequencies associated to lattice structure and phase transition were discussed from the experimental and theoretical results. The geometries, electronic structures and properties of both ZrO_2 and ZrO_2:6% Tb^{3+} systems have been characterized and discussed in relation to their crystal structural by using density functional theory (DFT) calculations.

2. Experimental section

2.1. Materials

Zirconium nitrate (Vetec, 99%), citric acid (Vetec), terbium nitrate (Aldrich, 99.9%), ethylene glycol (Synth, 99.5%) and distilled water were used as received to prepare the ZrO_2:Tb^{3+} particles.

2.2. Experimental process

The samples were prepared by **complex polymerization (CP)** method. In the synthesis process, zirconium citrate was obtained by dissolution of zirconium nitrate (Vetec, 99%) in an aqueous citric acid solution under agitation at an approximate temperature of 80 °C. The

Tb^{3+} cations were added for doping after complete dissolution of the zirconium nitrate, and the terbium nitrate was subsequently added (Aldrich, 99.9%). Ethylene glycol was employed to promote citrate polymerization through the polyesterification reaction, and the solution was constantly stirred. The molar ratio between citric acid and ethylene glycol was set to 60/40 (mass ratio). **The ratio of citric acid and metallic cation used in all syntheses was 6 mol% (CA): 1 mol% (Zr^{4+}).** Translucent resin was then formed 4 h after the water removal process. The dopant concentration was varied at 1,2,4 and 8 mol% Tb^{3+}. The polymeric resin was heat treated at 350 °C (10 °C/min) for 4 h, leading to partial decomposition of the polymeric gel and formed an expanded resin composed of partially pyrolyzed material. The particles were annealed at 500 °C for 2 h at a heating rate of 10 °C/ min.

2.3. Sample characterizations

The phases present in the ceramic powder were investigated by X-ray diffraction (XRD) using a Shimadzu XRD-7000 diffractometer with CuKα radiation. The diffraction patterns were analyzed by the general structure analysis system with an EXPGUI graphic interface [52] to perform the Rietveld refinement [53] and analyze the possible structural modifications. The following parameters were refined: scaling factor and phase fraction; background (displaced Chebyshev polynomial function); peak shape (Thomson-Cox-Hasting pseudo-Voigt); change in the network constants; fractional atomic coordinates; and isotropic thermal parameters. Micro Raman spectroscopy measurements were recorded using a *LabRAM HR Evolution spectrometer (Horiba, France)* with a triple monochromator coupled to a charge device detector. **The spectra were performed using a 633 nm wavelength of a He-Ne Laser complemented by argon ion laser,** keeping its maximum output power at 8 mW. **Raman spectroscopy measurements were performed in the range of 100 to 800 cm^{-1}.** The UV-vis reflectance spectra of the ZrO_2: Tb^{3+} particles were measured using Cary 5G equipment in the 200–800 nm range. PL spectra were obtained using a Thermal Jarrell-Ash Monospec 27 monochromator and a Hamamatsu R446 photomultiplier. The excitation source used on the samples was a laser at a wavelength of 350.7 nm with krypton ions (Coherent Innova) with an output of approximately 13.3 mW; all measurements were performed at room temperature.

2.4. Computational details

First-principle calculations at the DFT level were performed by using the Vienna *ab initio* simulation package (VASP). The Kohn-Sham equations were solved by using the Perdew, Burke, and Ernzerhof (PBE) exchange-correlation functional [54], alongside including the effect of long-range interactions using Grimme's D3 semi-classical dispersion methods [55]. The electron-ion interaction was described via the projector-augmented-wave pseudo potentials and the plane-wave expansion was truncated at a cut-off energy of 520 eV. The Brillouin zone was sampled by using $4 \times 4 \times 4$ Monkhorst-Pack special k-point grid to ensure geometrical and energetic convergence of the ZrO_2 structures. Both cubic and tetragonal phases of ZrO_2 undoped and doped at 6% Tb substitution were tested. The valence electron density is defined by 12 ($4s^2 4p^6 5s^2 4d^2$) electrons for Zr atoms, 6 ($2s^2 2p^4$) electrons for O atoms and 19 ($5s^2 5p^6 6s^2 4f^9$) electrons for Tb atoms. **A supercell with 96 atoms was used to simulate an amount of Tb doping up to 6% for both systems, $2 \times 2 \times 2$ and $2 \times 2 \times 4$ for cubic and tetragonal phases, respectively. In addition, a large supercell with 192 atoms was used to simulate an amount of Tb doping up to 3% for both systems, $4 \times 2 \times 2$ and $4 \times 4 \times 2$ for cubic and tetragonal phases, respectively.** Two Zr^{4+} were substituted by two Tb^{3+} and an oxygen vacancy was included to maintain the cell as electroneutral. The substitution process of Zr^{4+} by Tb^{3+} cations was done for both phases using structural models. The most energetically favorable arrangement can be selected to analyze theoretically the substitution

process.

The cell parameters and positions of all atoms were allowed to relax, and the conjugated gradient energy minimization method was used to obtain relaxed systems. This was achieved by setting a threshold value (i.e., 0.01 eV·Å^{-1}) for the forces experienced by each atom.

3. Results and discussion

Fig. 1 shows the XRD patterns of the ZrO_2 x mol% Tb^{3+} particles (x = 0,1,2,4 and 8%) prepared by the CP method. **For the analysis of the XRD, the standard powder diffraction cards with reference code JCPDS 81-1544 for tetragonal phase and JCPDS 89-9069 for cubic phase were used.** The Zr^{4+} cations in the tetragonal symmetry are coordinated by eight oxygen atoms, four oxygen atoms at a distance of 0.245 nm, and four other oxygen atoms at a distance of 0.206 nm. The ZrO_2 cubic shows fluorite symmetry, in which the Zr^{4+} cations are co-ordinated with eight oxygen atoms and the Zr−O bond length is 0.220 nm [35].

The difference between the tetragonal (metastable) and cubic phase based only on the XRD analysis becomes inaccurate because the ratio between the lattice parameters (c / $\sqrt{2}$a) for both phases is similar ($\approx$ 1) [56]. According to Shukla et al [57], this oxygen-induced transition cannot be detected by XRD owing to the small scattering factor of the oxygen atom.

Fig. 2 **represents the XRD of samples ZrO_2 and ZrO_2: 8% Tb performed in a scan of 0.02°/min. It is possible to identify changes in the characteristics of the diffraction peaks in the regions between 56 and 64° and between 71 and 76°. It is verified for sample ZrO_2 the presence of the division of the peaks represented by the planes (211) and (202) in 59.76° and 62.65° respectively in** Fig. 2 **(b) and (004) and (220) in 72.90° and 74.41° respectively in** Fig. 2 **(d) characteristic of the tetragonal phase. For the ZrO_2: 8%Tb sample, is observed the presence of peaks (311) and (400) located at 59.20°** (Fig. 2(c)) **and 73.40°** (Fig. 2(e)) **respectively, characteristic of the cubic phase. There are also peaks not well defined in (202) and (004) located at 62.5° and 72° respectively, attributed to the tetragonal phase. Comparing the peak intensities for the planes (202) and (004) for ZrO_2 and ZrO_2:8% Tb samples, there is a significant decrease in intensity for the ZrO_2:8% Tb samples. The intensity of the plane (202) for ZrO_2 is 0.060, while the intensity of the plane (202) for ZrO_2: 8%Tb decreases to 0.044. The plane intensity (004) for ZrO_2 is 0.016, in contrast the plane intensity (004) for ZrO_2: 8%Tb decreases to 0.009. It is reasonable to assume that**
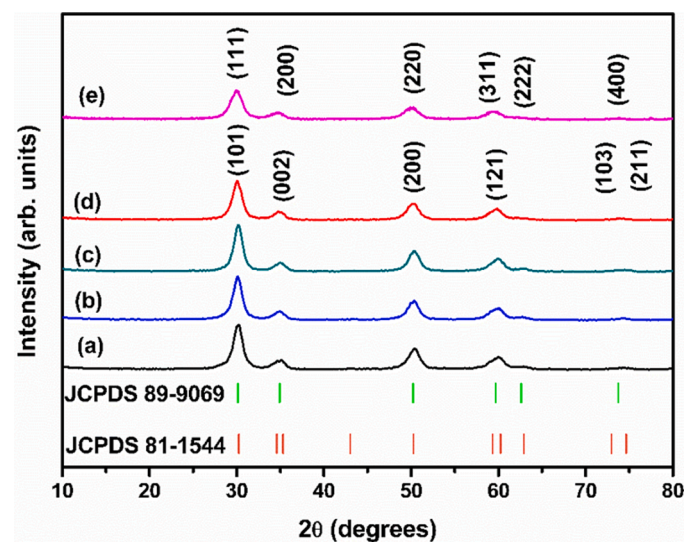
at 8% Tb the phase transition from zirconia to the cubic phase is already occurring, coexisting with the tetragonal phase, the latter in smaller amounts. Vasanthavel and Kannan [58] detect the tetragonal - cubic phase transition of itrium doped ZrO_2 observing a gradual change in the peak profile.

Rietveld refinements were performed to confirm the obtained crystalline phase and the lattice parameter values and atomic positions of ZrO_2: x mol% Tb^{3+} (x = 0,1,2,4, and 8%) samples are presented in **Table S1 in the supplementary information. Fig. S1 in the Support Information** shows a schematic representation of the crystalline structures. The size of the sample crystallites was estimated from the Scherrer equation and the full-width half-maximum (FWHM) of an observed peak. The average crystallite size (D) of ZrO_2:Tb^{3+} powders was determined from the strongest peaks corresponding to the (101) tetragonal phase and (111) cubic phase.

Small changes in the lattice parameters were observed between the samples due to the substitution of $Zr^{4+} \rightarrow Tb^{3+}$ in the ZrO_2:Tb^{3+} and as a result a variation in the crystallite size and distortion in the Zr-O bond length. The cell volume increases as the amount of dopant increases due to the ionic radius of Tb^{3+} (1.04 Å) [59] being greater than the ionic radius of Zr^{4+} (0.72 Å) [60].

It is observed that the values of the lattice parameters "*a*" and "*c*" change due to the increase in the concentration of Tb^{3+} in the ZrO_2 lattice and there is no evidence of linearity between these two structural parameters as predicted by Vegard's law [61,62]. This discontinuity can be associated with structural defects and distortions within the ZrO_2 lattice. An analysis of the results renders that a decrease of the *c/a* ratio in the tetragonal ZrO_2 lattice can be sensed as the amount of Tb^{3+} increases. **A similar behavior can also be seen in studies [63,64].** Kumar et al. [63] states that the addition of Ce^{4+} to ZrO_2 promoted a reduction in asymmetry in the tetragonal phase. Certifying a decrease in the $c/\sqrt{2}a$ ratio by the influence of Ce^{4+} due to the introduction of oxygen vacancies in the host lattice. The emergence of vacancies is a mechanism to maintain the neutrality of material charges.

DFT calculations were carried out to investigate the doping process at **3% and 6%** of Tb^{3+} in cubic and tetragonal ZrO_2 phases. The most stable geometries are shown in Figs. 3 and 4.

An optimized structure with Tb^{3+} cations near each other is the most stable atomic arrangement for the cubic phase. Fig. S2 in the supplementary information shows the remaining cubic arrangements studied, displaying less stability. Different Tb^{3+} arrangements show similar energy for the tetragonal phase. The difference between the formation energies of the cubic and tetragonal phases (ΔE_{C-T}) of ZrO_2, **$Zr_{0.97}Tb_{0.03}O_{1.97}$ and $Zr_{0.94}Tb_{0.06}O_{1.94}$ are 0.84 eV, 0.65 eV** and -0.33 eV, respectively. **These results indicate that for pure ZrO_2 and 3% doped-ZrO_2 the tetragonal structure is more stable than cubic structure.** The incorporating 6% Tb^{3+} into the ZrO_2 structure increases the stability of the cubic phase relative to the tetragonal phase, and a more favorable substitution occurs in the cubic polymorph of ZrO_2 as the amount of Tb^{+3} increases. This substitution maintains a structural symmetry in the cubic polymorph (one Tb^{3+} away from each other), as can be seen in Fig. S2, in which a less stable arrangement can be observed, and the phase transition from tetragonal to cubic is not observed.

The difference in the electron density of Zr^{4+} in relation to Tb^{3+} at 6% substitution induces distortion in the crystalline lattice of ZrO_2. In addition, the results presented in Table 1 show that the substitution process provokes a local distortion in both the cubic and tetragonal structures which are both centered on the dopant and located near the oxygen vacancy (V_o), as previously reported [24]. The introduction of Tb^{3+} to the Zr^{4+} site promotes an accumulation of negative charge, with concomitant appearance of oxygen vacancies (V_o) as a load balancing mechanism [45].

The calculated values of the cell parameters at 6% Tb^{+3} are in good agreement with the experimentally determined results **collected in**
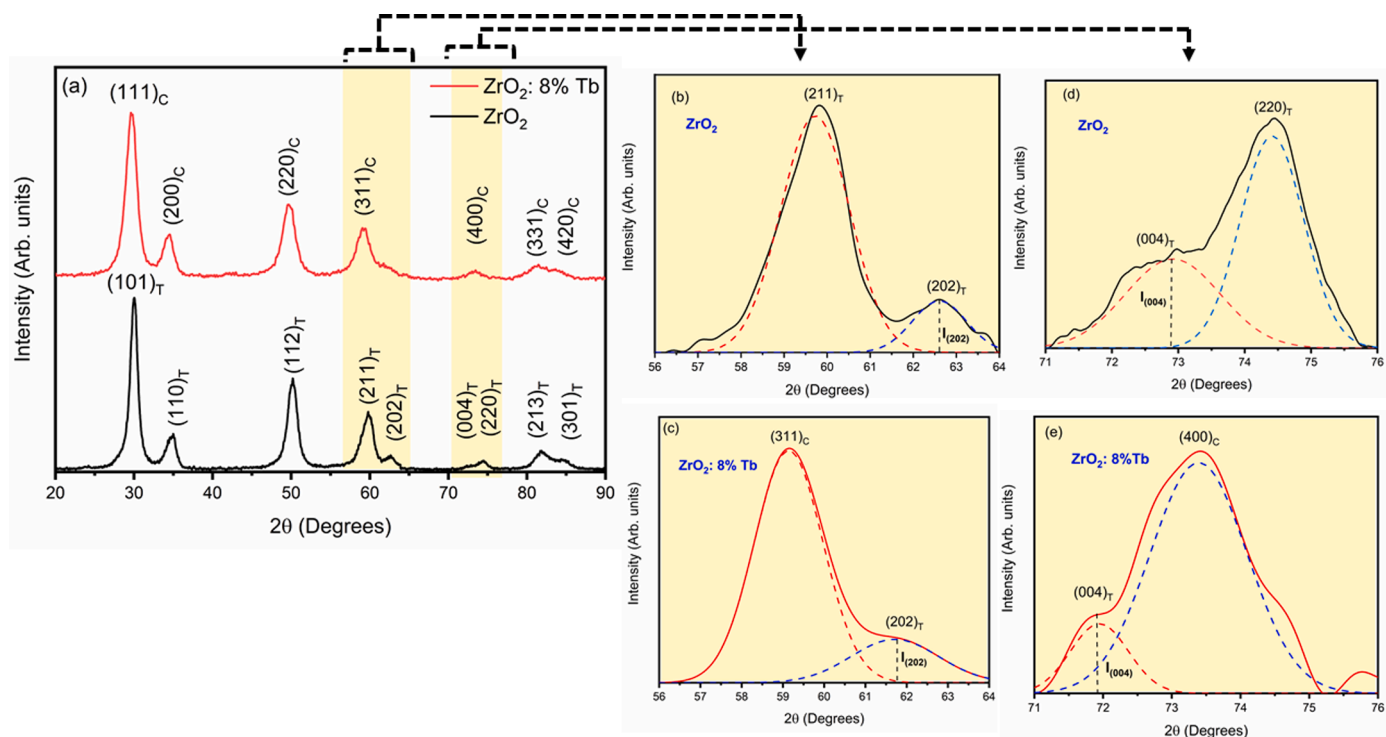

Fig. 1. XRD patterns of ZrO_2: x mol% Tb - (a) x = 0, (b) x = 1, (c) x = 2, (d) x = 4 and (e) x = 8.

Fig. 2. XRD of ZrO$_2$ and ZrO$_2$: 8%Tb samples performed in a scan of 0.02°/min: (a) 2θ = 20–90°; (b) 2θ = 56–64° for ZrO$_2$; (c) 2θ = 56–64° for ZrO$_2$: 8%Tb; (d) 2θ = 71–76° for ZrO$_2$; (e) 2θ = 71–76° for ZrO$_2$: 8% Tb.

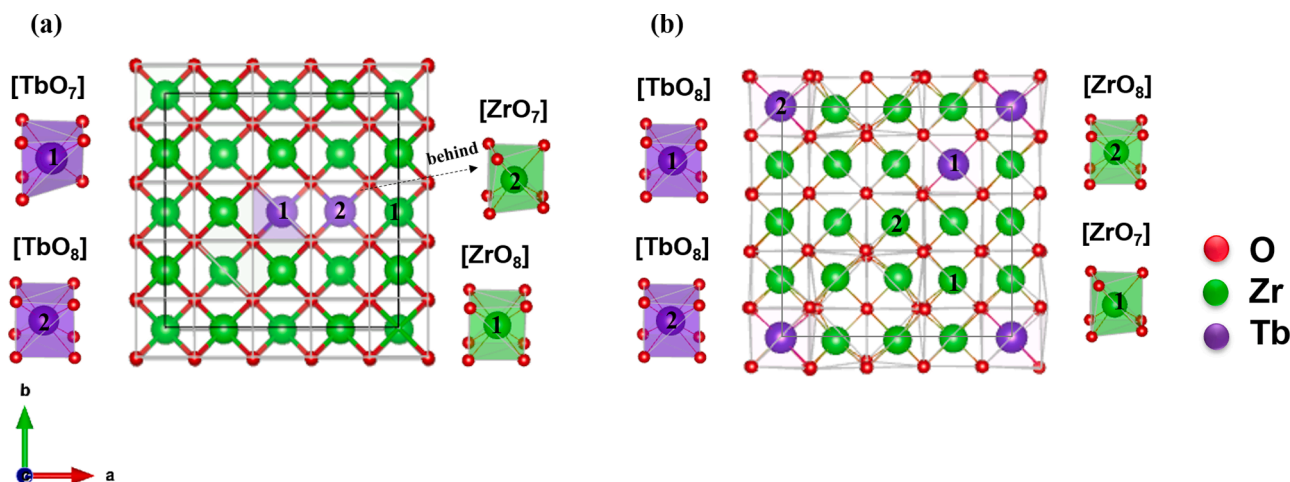**Fig. 3.** Cubic structure of ZrO$_2$: (a) 3% and (b) 6% Tb^{3+}. The cluster coordination of the [TbO$_8$], [TbO$_7$], [ZrO$_8$] and [ZrO$_7$] are highlighted.

Table S1 (a = 5.254 Å for the cubic phase, and a = 3.651 Å and c = 5.285 Å for the tetragonal phase).

The transformation from the tetragonal phase to the cubic phase as a result of the introduction of Tb^{3+} ions into the ZrO$_2$ lattice can be observed by analyzing the Raman spectra of Fig. 5. The bands located in the spectra (a–d) of Fig. 5 in: **147, 266, 317, 462 and 640** cm^{-1} are characteristic bands of the tetragonal phase [43,46,50,65]. **The Raman bands associated with the ZrO$_2$ tetragonal phase are represented by six active modes (A$_{1g}$ + 2B$_{1g}$ + 3E$_g$) [66]. The bands observed at 147, 266 and 462 cm^{-1} are assigned to Eg mode. The bands located at 317 and 640 cm^{-1} refer to the B$_{1g}$ mode. It was not possible to identify the active mode A$_{1g}$ in the Raman spectra.** The Raman E$_g$ (150 cm^{-1}) and B$_{1g}$ (312 cm^{-1}) active modes are associated with the movement of the Zr sublattice. The Raman mode located at 642 cm^{-1} corresponds to the asymmetric bending vibrations of the Zr-O-Zr moiety

[67]. In contrast, the cubic phase can be clearly characterized by a relatively wide band between 533 and 664 nm centered on 625 cm^{-1} [65,68]. It is observed that there is a gradual reduction in the tetragonal phase percentage with the increase in the Tb^{3+} concentration. Meanwhile, the cubic phase percentage gradually increases. **A shift of the 625 cm^{-1} band to a smaller region in the ZrO$_2$: 8%Tb sample is observed when compared to the ZrO$_2$: x% Tb (x = 0,1,2 and 4) samples which occurs at 640 cm^{-1}. This change in behavior is characteristic of the cubic phase, as evidenced by Vasanthavel et al. [69].**

Shukla et al [57] relate the E$_{g(3)}$ mode in 462 cm^{-1} to the presence of a metastable tetragonal phase of ZrO$_2$ (t'- ZrO$_2$). This band is subtly verified in the Raman spectrum of the ZrO$_2$: 8% Tb sample. Indicating the coexistence of the two phases: cubic (c-ZrO$_2$) and metastable tetragonal (t'- ZrO$_2$). The t'- ZrO$_2$ phase is
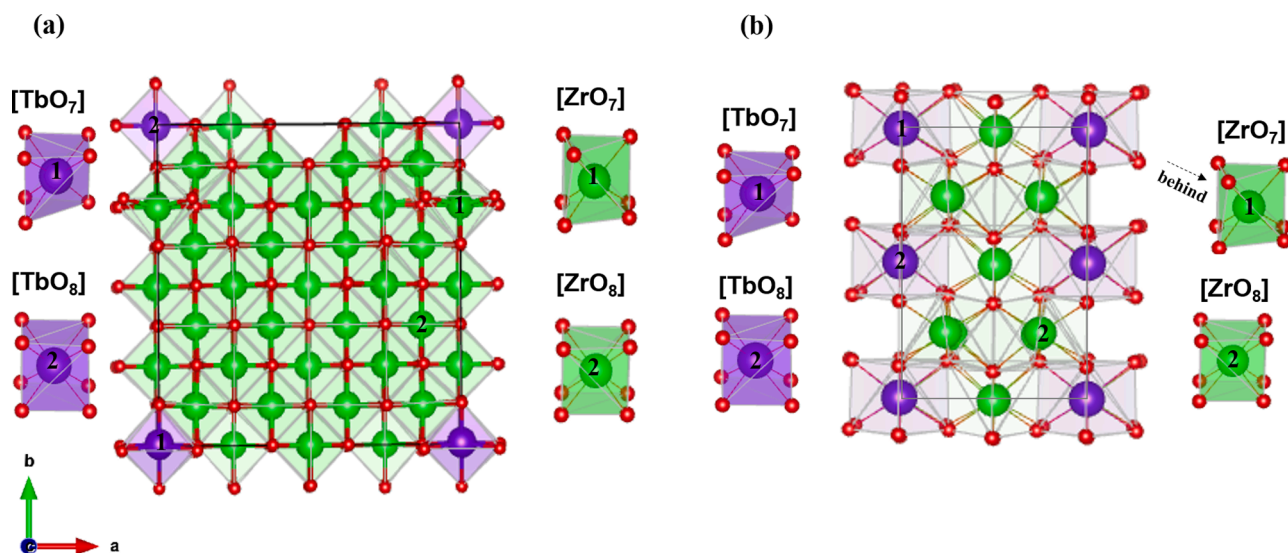
(a)   **(b)**

Fig. 4. Tetragonal structure of ZrO_2: (a) 3% and (b) 6% Tb^{3+}. The cluster coordination of the $[TbO_8]$, $[TbO_7]$, $[ZrO_8]$ and $[ZrO_7]$ are highlighted.

Table 1

Zr-O and Tb-O distance values at 6% Tb^{3+} substitution in the cubic and tetragonal ZrO_2 structures.

Cubic_6%			Tetragonal_6%		
Atom	Coord.	Bonds (Å)	Atom	Coord.	Bonds (Å)
Zr1	7	2.180	Zr1	7	2.334
		2.190			2.063
		2.142			2.063
		2.164			2.042
		2.176			2.400
		2.106			2.074
		2.159			2.400
Zr2	8	2.173	Zr2	8	2.155
		2.209			2.512
		2.224			2.155
		2.214			2.484
		2.179			2.345
		2.217			2.077
		2.335			2.345
		2.214			2.073
Tb1	8	2.312	Tb1	7	2.281
		2.326			2.348
		2.290			2.281
		2.289			2.245
		2.294			2.348
		2.309			2.209
		2.326			2.348
		2.312			-
Tb2	8	2.326	Tb2	8	2.351
		2.462			2.294
		2.352			2.352
		2.324			2.294
		2.298			2.326
		2.326			2.347
		2.324			2.470
		2.315			2.347

Fig. 5. Raman spectra of: (a) pure ZrO_2 (tetragonal phase); (b) ZrO_2:1 mol% Tb^{3+} (tetragonal phase), (c) ZrO_2:2 mol% Tb^{3+}, (d) ZrO_2:4 mol% Tb^{3+} (tetragonal phase), (e) ZrO_2:8 mol% Tb^{3+} (cubic phase + t'- ZrO_2).

characterized by having a distorted shape of the cubic phase. Although, the relation of the lattice parameters ($c /\sqrt{2}a \to 1$) are similar in both phases; in the t'- ZrO_2 phase, the oxygen ions are shifted alternately (zigzag aspect) along the z axis, assuming tetragonal symmetry [57]. Fujimori et al. [70,71] describe the structural evolutions of ZrO_2 by measuring the displacements of oxygen ions on the z axis considering the relationship of the intensity of the bands $E_{g(3)}$ (462 cm^{-1}) and B_{1g} (640 cm^{-1}) named, respectively, by I_4 and I_5 in Fig. 6.

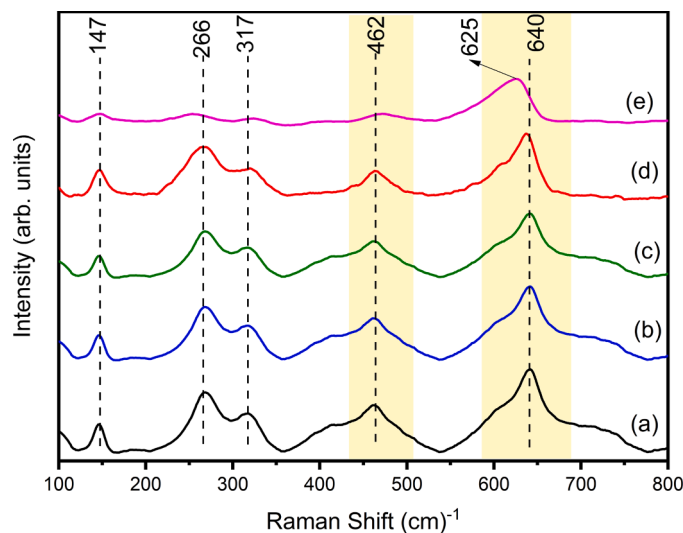Fig. 6 shows the changes registered in the bands $E_{g(3)}$ (462

cm^{-1}) and B_{1g} (640 cm^{-1}) in the Raman spectra in the range of 350 to 800 cm^{-1} for the samples: ZrO_2, ZrO_2: 4% Tb and ZrO_2: 8% Tb. Spectrum adjustments were made from the Lorentzian profile (R^2 = 0.99). The ratio of the intensity of the I_4/I_5 bands to ZrO_2, ZrO_2: 4% Tb and ZrO_2: 8% Tb are 0.558, 0.403 and 0.130 respectively. The effect of increasing the concentration of Tb^{3+} in ZrO_2 promotes a decrease in the I_4/I_5 ratio. Considering a decrease in the displacement of the oxygen ion along the z axis within the unit cell, and as a consequence, a reduction in tetragonality. According to the results presented, it is reasonable to consider that the majority phase for ZrO_2: 8% Tb is cubic. The active Raman modes for the crystal structures of ZrO_2 are shown in Table 2. At this point, it is important to note that the cubic and tetragonal phases of ZrO_2 present similar XRD diffraction peaks, and therefore the relative fraction of each phase along the samples cannot obtained.

According to Jomard et al. [72], the cubic structure is a special case of the tetragonal structure and can be obtained from it, making the ratio of the lattice constants $c/\sqrt{2}\,a \to 1$. This statement is in accordance with the values ($c /\sqrt{2}\,a$) presented in **Table S1**. In the transformation of the
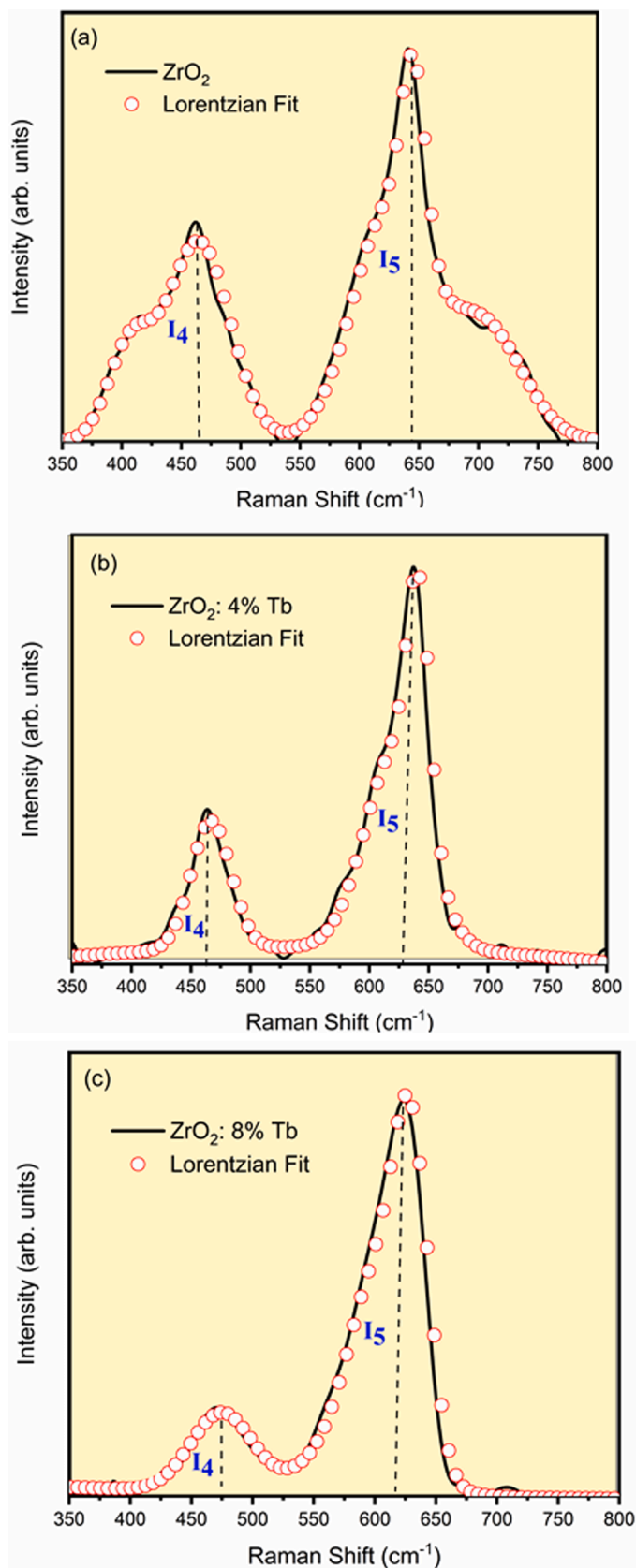
Fig. 6. Raman spectrum in the range 350 to 800 cm^{-1}. Evaluation of structural changes; ratio of I_4/I_5 intensities.

Table 2
Raman active mode, space group of the different ZrO_2 phases.

Crystalline system	Space group	Raman modes	c/a ratio
Monoclinic (m)	C_{2h}	$9A_g + 9B_g$	-
Tetragonal (t)	D_{4h}	$A_{1g} + 2B_{1g} + 3E_g$	> 1
Cubic (c)	O_h	T_{2g}	$= 1$

tetragonal → cubic phases, the pairs of oxygen atoms are displaced from the z direction to their central positions in the unit cell [72]. The fundamental difference in the zirconia phase structure is due to the displacements of oxygen atoms in the lattices. The doping effect is important to determine the stabilization of the ZrO_2 phases. According to Tiseanu et al. [67], the main structural difference between the zirconia phases refers to the displacements of oxygen atoms in the lattices, thus signaling that the importance for local atomic structure is fundamental for understanding the effect of doping process on ZrO_2.

However, Wang et al. [73] show that the location and concentration of oxygen vacancies in yttria-stabilized zirconia can be determined by measuring atomic displacements of the cationic sub-lattice. According to the DFT calculations performed by the group, the alternating presence of oxygen vacancies in the locations (1/4, 1/4, 1/4) and (1/4, 3/4, 1/4) along the direction [001] that promotes the atomic displacements of the cationic sub-lattice. The cation displacements from the ideal face-centered cubic (FCC) sites are related to the relaxation of the neighboring cations away from the vacancies. When an oxygen vacancy is created, the neighboring cations will repel each other because of Coulombic interactions, thereby resulting in larger distance between cátions [73].

Theoretical calculations of the Raman-active modes of pure tetragonal ZrO_2 yielded values of 149.4, 294.2, 301.5, 453.6, 611.5, and 650.9 cm^{-1} for the E_g, A_{1g}, B_{1g}, E_g, B_{1g}, and E_g modes, respectively. The case of pure cubic ZrO_2 (a unique mode which has T_{2g} symmetry) occurs at a wavenumber of 600.7 cm^{-1}. These values agree with previous values reported by our research group [24].

The band gap energy (E_{gap}) of the ZrO_2:x mol% Tb^{3+} sample was estimated from the Uv-visible measurements by plotting the square of the Kubelka-Munk function $[F(R)^2]$ versus (eV), extrapolating the linear part of the curve to the condition of $F(R)^2 = 0$ [74], according to Eq. (1):

$$F(R) = \frac{k}{s} = \frac{(1-R)^2}{2R} \tag{1}$$

where R is the percentage of reflected light. The incident photon energy ($h\nu$) and the gap energy (E_{gap}) are related to the transformed Kubelka-Munk function (2):

$$[F(R)h\nu]^n = A(h\nu - Egap) \tag{2}$$

where A is a constant which depends on the probability of the transition and n is the index that is related to the optical absorption process. We can then assume the following values: ½ or 2 for direct and indirect allowed transitions, respectively. The transition in the case of ZrO_2 is considered to be the direct type. It is necessary to observe the energy conservation in the crystal for a material to have direct electronic transitions. This condition is reached when the valence band (VB) maximum and the conduction band (CB) minimum are positioned in the same symmetry region of the solid. It is observed that the gap energy decreases as the Tb^{3+} concentration increases as the E_{gap} values remained between 5.11 and 4.92 eV, as shown in Fig. 7.

The effect of the band gap narrowing due to the doping process is well known in semiconductors [75]. This phenomenon happens due to the presence of defects inside the band gap which promotes the appearance of intermediate levels. **Oxygen vacancies appear to compensate for the Zr^{4+} ions replaced by Tb^{3+} ions. Due to the difference in charge of cations, oxygen waves are formed as a mechanism for charge neutrality in the material. The defect reaction equation can be described in the following Eq. 3:**
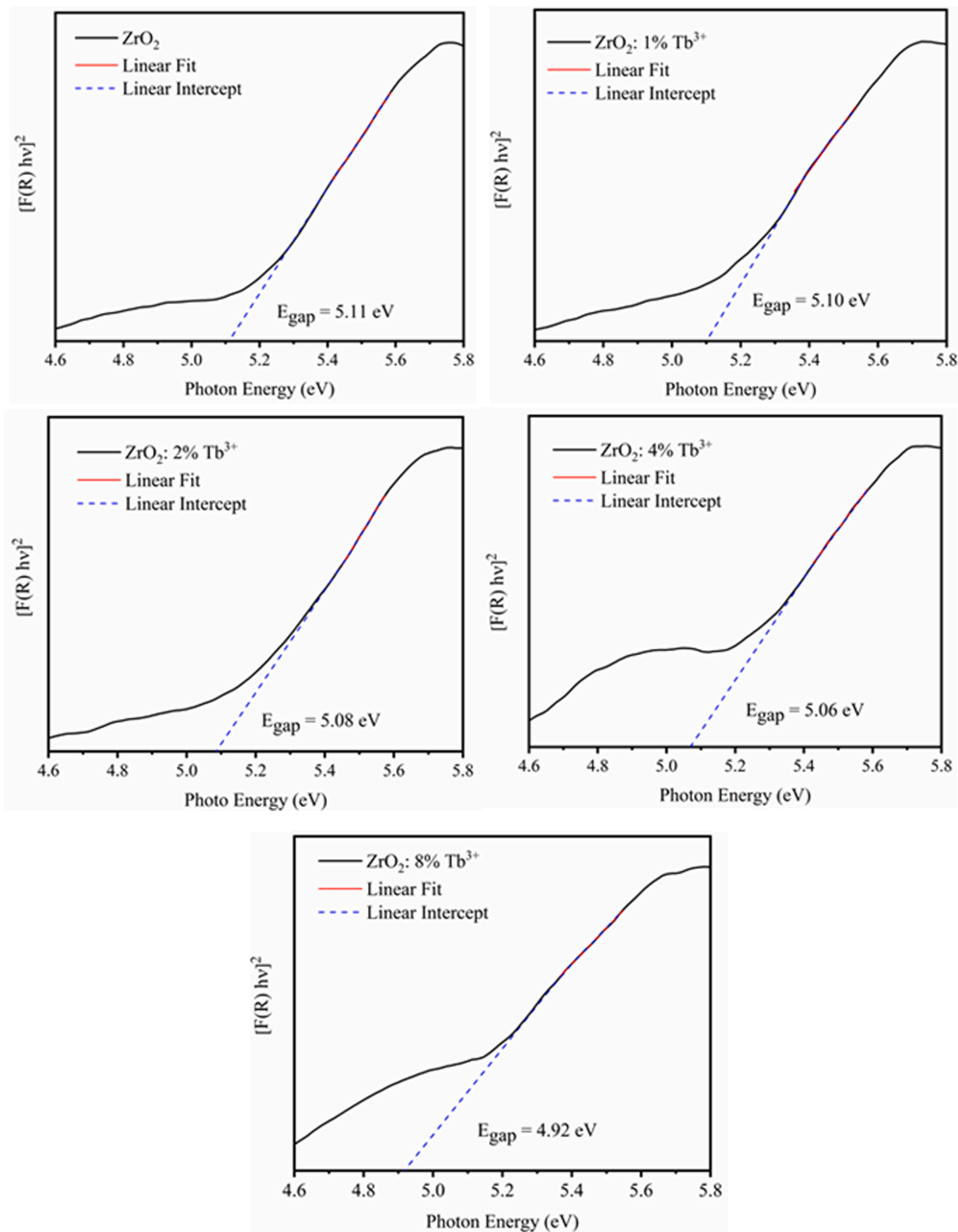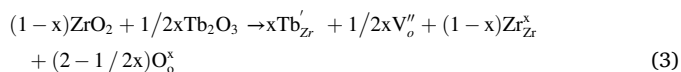
Fig. 7. Determination of the band gap for ZrO_2: x mol% Tb^{3+} (x = 0,1,2,4 and 8).

$$(1-x)ZrO_2 + 1/2xTb_2O_3 \rightarrow xTb'_{Zr} + 1/2xV''_o + (1-x)Zr^x_{Zr}$$
$$+ (2-1/2x)O^x_o \qquad (3)$$

where T'_{Zr}, means Tb^{3+} occupying the normally occupied by a Zr^{4+} due to replacement by Tb^{3+}. V''_o is the O^{2-} vacancy. Zr^x_{Zr} represents the rest zirconium in the lattice of ZrO_2 and O^x_o is the oxygen in the lattice of ZrO_2. At low concentrations of Tb^{3+}, there is little V''_o ZrO_2, and the symmetry of the host structure is not seriously influenced. The larger the concentration of Tb^{3+} in the host, higher the number of oxygen vacancies is able to create a new surrounding in the host. The new surrounding disturbs the symmetry of the host. Donor-type defects are located close to the conduction band, while the acceptor-type defects generate energy levels near the valence band. As the Tb^{3+} concentration increases, the density of intermediate energy states in the band gap interval increases [45], with a concomitant decrease of the band gap.

The total and projected density of states (DOS) of the atoms for the 6% doped cubic and tetragonal phase are shown in Fig. 8. E_g values for undoped cubic and tetragonal phases of 3.21 eV and 3.83 eV, respectively, were previously reported [24], with the top of the VB and the bottom of the CB mainly being composed of O 2p levels and Zr 4d levels, respectively. These values are both lower than their experimentally determined counterparts, a well-known underestimation of the PBE functional. A comparison of the electronic structures shown in Fig. 8(a) and 8(b) reveals that Tb doping leads to a systematic decrease in E_g to 2.05 eV and 2.35 eV, respectively, and an increase in the density of electronic states inside the gap. Therefore, the theoretical calculations indicate that these states occur in the forbidden energy zone owing to the presence of Tb transition metals and O vacancies in the ZrO_2 lattice.

It is possible to study the electronic structure of the materials from the analysis of PL spectra (levels of impurities and probable defects in the materials to identify recombination mechanisms of charge carriers - electron-gap pairs - within the band gap) [76]. Fig. 9 shows the PL emissions of ZrO_2 excited at a wavelength of 350 nm at room temperature. There is a broadband profile between 350 and 700 nm with a maximum of 460 nm. The broadband characteristic is associated with a multiphonic process behavior. Electronic transitions are the result of relaxation and recombination processes which involve several stages and states located in the material band gap [77].

The broadband profile shown in Fig. 9 is characteristic of the contribution of several luminescent bands which overlap and exhibit a continuous spectrum according to other works [26,78]. The presence of defects and vacancies in the materials promote the appearance of energy

levels located in the band gap. These levels are associated with the distribution of charges around each component of the crystalline lattice. These loads can be distorted according to the concentration of defects present [79,80]. The PL emissions can be understood from the following considerations: (a) impurities, (b) intrinsic self-trapped excitons, and (c) intrinsic defects, such as F-centers and Zr^{3+}-centers [81–83]. Different types of defects can generate different types of electronic transition states in the gap region. Defects which form levels close to the condition or valence ranges are called surface defects. The defects that cause the appearance of transition states far from the valence and conduction bands are classified as deep defects [84]. Theoretical studies performed on ZrO_2 have evaluated the stability of surface defects and deep defects in the different crystalline structures of ZrO_2 [85,86] and have clarified the luminescent emission resulting from oxygen vacancy states in the ZrO_2 lattice. Oxygen vacancies introduce states located in the ZrO_2 into the gap which result in various emission states [82,85].

Spectrum deconvolution was performed using the Peak fit 4.12 program to estimate the contribution of each visible band to the overall color composition emitted by the sample. The spectrum was decomposed into three curves under the following conditions: 54% blue (λmax = 472 nm), 36% (λmax = 550 nm) and 10% (λmax = 630 nm).

The intensity of the photoluminescence of rare earth ions (RE^{3+}) is essentially controlled for two important reasons: first, the extent of non-radioactive deactivation (quenching) of the excited state of the RE^{3+} ion and second, the competence of the excited state of the host matrix (triplet) to transfer energy to the RE^{3+} ion emission state. These factors are influenced by the nature of the RE^{3+} ion, by the matrix, by the connection between the RE^{3+} ion and the matrix [87,88].

Fig. 10 shows the PL spectra at room temperature of the ZrO_2:x mol% Tb^{3+} (x = 1,2,4,8) particles. The spectra show the intraconfiguration $^5D_4 \rightarrow {}^7F_J$ (J = 3,4,5 and 6) transitions of the Tb^{3+} ion located at: 625, 590, 550 and 500 nm, respectively. The effect of Tb^{3+} concentration on PL intensity was evaluated. It is verified that the maximum intensity of PL was obtained by the ZrO_2:2 mol% Tb^{3+} sample, as shown in the inset of Fig. 10, precisely for the $^5D_4 \rightarrow {}^7F_5$ transition (λ = 550 nm). The $^5D_4 \rightarrow {}^7F_5$ transition is the most intense for all samples; this behavior indicates that there is a predominance of the electric domain [45]. Fig. 10 (b) shows an illustration of how the concentration interferes with the PL intensity. Small Tb^{3+} concentrations in the ZrO_2 matrix generate an increase in PL intensity, while a decrease can be observed at the top of the critical concentration where the Tb^{3+}-Tb^{3+} interactions appear (quenching region).

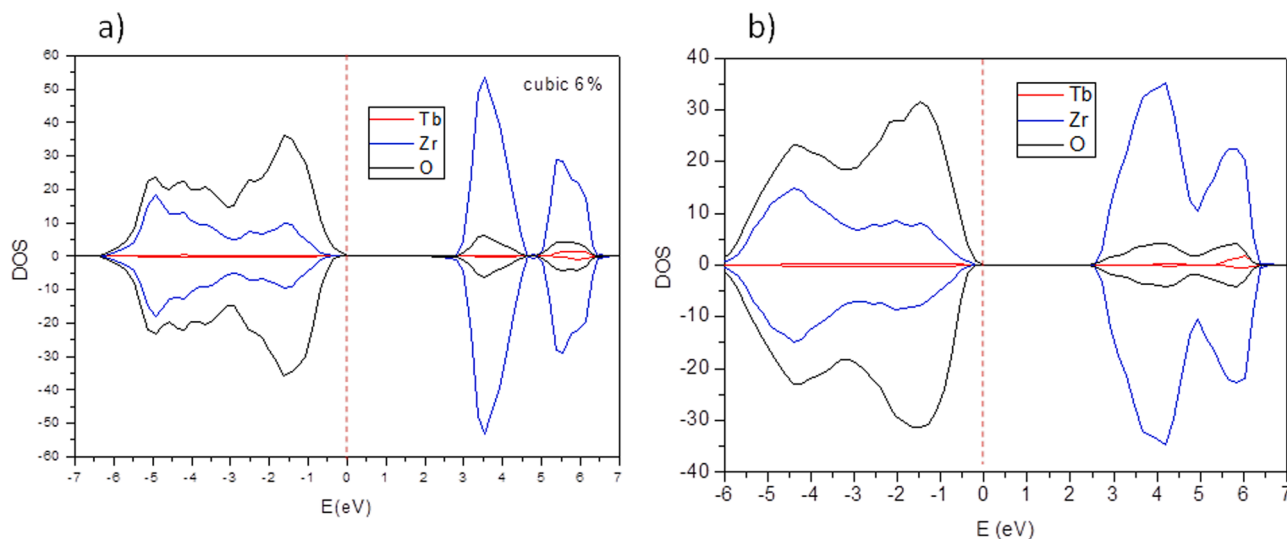The electrostatic interaction between Tb^{3+} ions becomes larger for

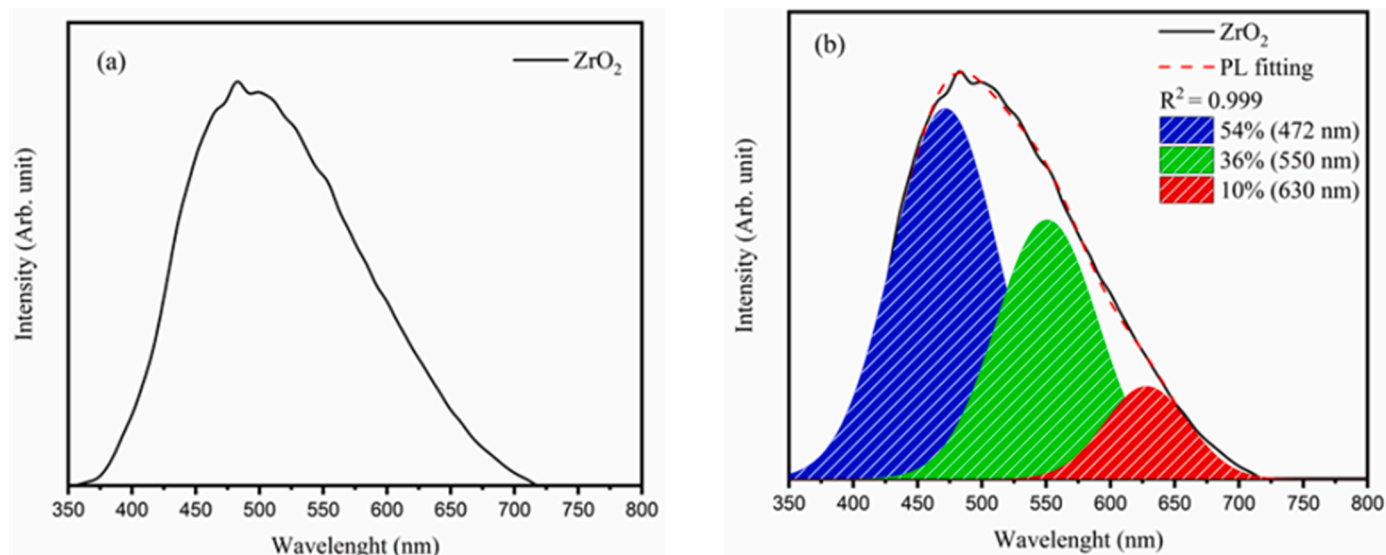**Fig. 8.** Projected density of states on the 6%Tb-doped atoms of cubic (a) and tetragonal (b) phases.

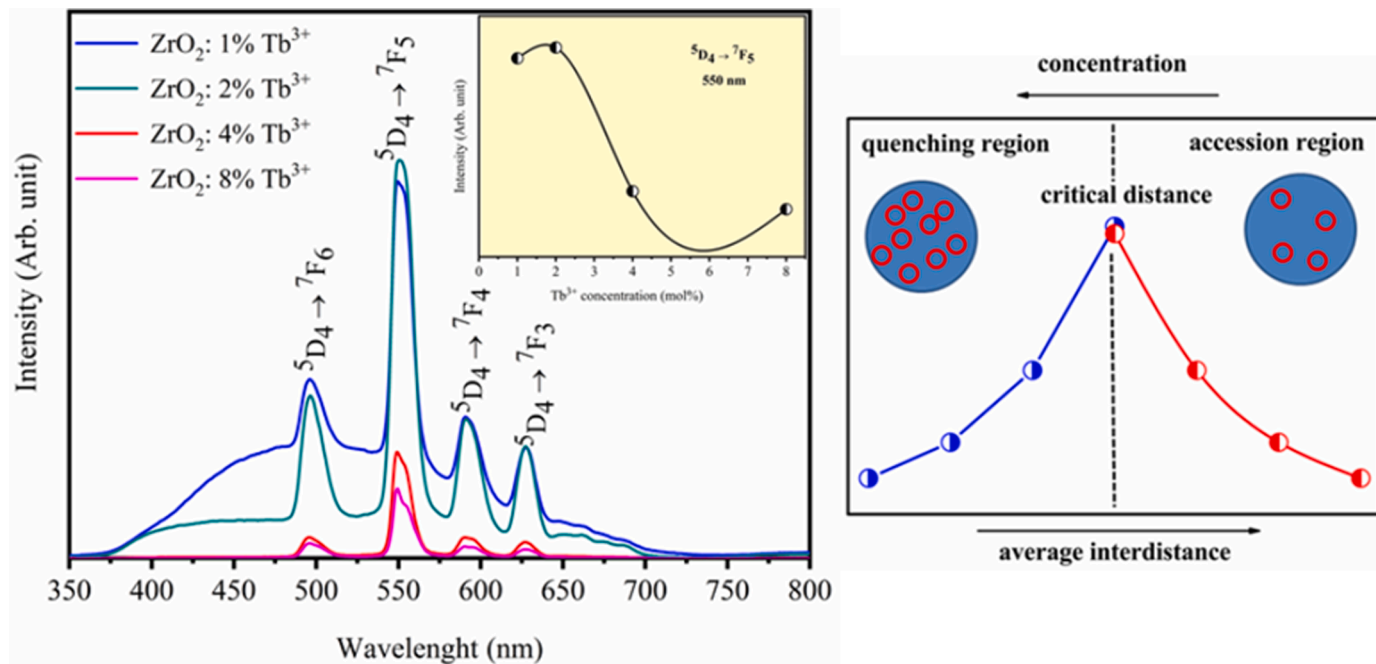**Fig. 9.** ZrO$_2$ emission spectrum; λ_{exc} = 350 nm

Fig. 10. Emission spectra of ZrO$_2$:x mol% Tb^{3+} (x = 1,2,4 and 8) particles.

concentrations greater than 2 mol% Tb^{3+} due to the shortened distance between neighboring Tb^{3+} ions. This results in favoring non-radiative transitions and in turn, causes suppression of PL emissions. The critical distance (Rc) between the neighboring Tb^{3+} ions leads to the quenching effect. The Rc was estimated from the Blasse Eq. (4) [89]:

$$\mathbf{Rc} \cong 2\left(\frac{3\mathbf{V}}{4\mathbf{Xc}\pi\mathbf{Z}}\right)^{1/3} \tag{4}$$

Where V is the volume of the unit cell, Xc is the critical concentration of Tb^{3+}, and Z is the number of atoms per unit cell. The terms for ZrO$_2$:2 mol% Tb^{3+} assume the following values: V = 67.4481 (Å)^3, Xc = 0.02 mol and Z = 4. The estimated value of Rc = 15.8 Å; as Rc is greater than 5 Å, this means that the energy transfer process occurs through multipolar interactions [90]. These types of interactions are responsible for suppressing the PL emissions and can be classified as: dipole-dipole or quadrupole-quadrupole interactions.

The host matrix plays a particularly important role along the PL processes. It has the ability to absorb the excitation energy due to its favorable band structure and subsequently transfer some of this energy to the activating ions (Tb^{3+}). Thus, it acts as a sensitizer. The main characteristics of the host matrix which guarantee efficient energy transfer are strong absorption, low phonon energy and photochemical stability. Fig. 11 shows a sensitizer (ZrO$_2$)-activator (Tb^{3+}) model for energy transfer and photon emission. ZrO$_2$ absorbs the excitation energy, and part of this energy is transferred to the ^{5}L$_{10}$, ^{5}D$_2$, ^{5}D$_3$ and ^{5}D$_4$ levels of Tb^{3+}, and later the characteristic emissions of Tb^{3+}, ^{5}D$_4 \rightarrow ^7$F$_J$ (J = 0–6) occur.

The chromaticity coordinates (Xc, Yc) were calculated according to the spectra distribution. Fig. 12 shows the chromaticity plot, wherein it is observed that the increase in Tb^{3+} concentration exhibits an emission
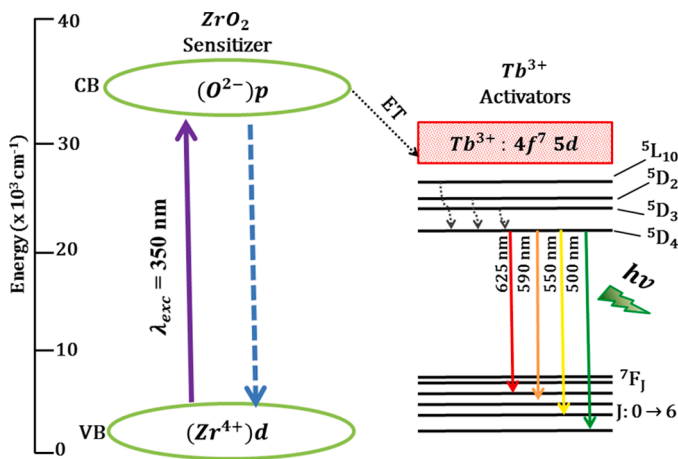
Fig. 11. Illustration of the level diagram, energy transfer and Tb^{3+} transitions.
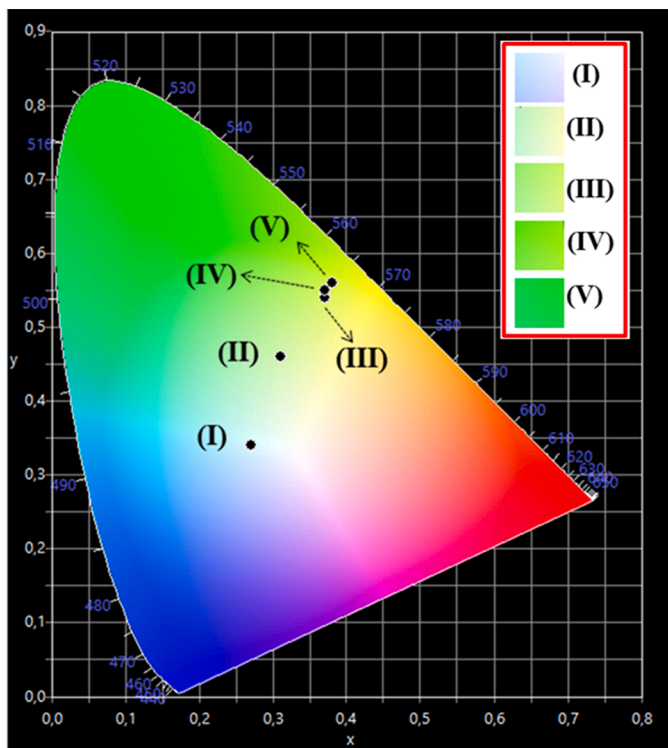

Fig. 12. Chromaticity diagram.

tendency in the green region. The purity degree of the color was evaluated, verifying that the increase in the Tb^{3+} concentration promotes growth in the purity percentage of the green color. Color purity was calculated from Eq. (5) [91]:

$$olor\ purity\ \% = \left(\frac{\sqrt{(x-xi)^2 + (y-yi)^2}}{\sqrt{(xd-xi)^2 + (yd-yi)^2}} \right) \times 100\% \qquad (5)$$

where (x, y) are the sample point coordinates, (xd, yd) are the dominant wavelength coordinates ($\lambda = 550$ nm) and (xi, yi) are the white light coordinates in the diagram. In the present study (xd, yd) = (0.60, 0.40) and (xi, yi) = (0.3101, 0.3162).

The correlated color temperature (CCT) values for the doped samples were not possible to determine because they are distant from the

temperature line (K) according to their chromaticity coordinates, and their indication becomes irrelevant under these conditions. The color reproduction index (CRI) was also investigated, for which the non-doped ZrO_2 presented better results with 78% color reproducibility. Table 3 shows all the values referring to the parameters which characterize the colors exhibited by the samples.

The luminous efficiency of radiation (LER) of the samples was also investigated, for which the results showed high LER values (521 lm. W^{-1}), constituting a desired characteristic for use in WLEDs. The ratio of the emitted luminous flux in lumen and the power used in watts describes the LER. The LER is a measure of how brightly the radiation is perceived to be by the average human eye expressed in lumens per visible watts. It is observed that the increase in the Tb^{3+} concentration promotes an increase in LER.

4. Conclusions

The ZrO_2:xTb^{3+} (x = 1,2,4 and 8 mol%) samples of green phosphor were successfully synthesized by the complex polymerization method. The effect of the Tb^{3+} doping process on the luminescence performance and phase transition (cubic vs tetragonal) were investigated by XRD, and Raman and diffuse reflectance spectroscopies. In addition, first-principle calculations at the density functional theory level were performed to understand the effects of the doping process of Tb^{3+} (**3 and** 6%) in tuning the electronic and optical properties on ZrO_2. The main conclusions of the present work can be summarized as follows: (i) An enhanced green emission is observed as Tb^{3+} is introduced to the ZrO_2 lattice due to the more intense $^5D_4 \rightarrow {}^7F_5$ transition around 550 nm; (ii) Color purity was tunable from the addition of Tb^{3+}, reaching 80.5% for the ZrO_2:8 mol% Tb^{3+} sample; (iii) The quenching effect was evaluated and it was concluded that the optimum concentration for maximum PL intensity was 2 mol% Tb^{3+}; (iv) the present findings indicate that the ZrO_2:x mol % Tb^{3+} sample is a promising new green phosphor material which is applicable to solid state lighting devices.

5. Prime Novelty Statement

This study provides a fundamental and thorough investigation regarding the synthesis, characterization and optical properties of ZrO_2: xTb^{3+} with high availability for optical applications. Through a control in the synthesis conditions, and in the chemical composition of the materials it was possible to optimize the responses to photoluminescence properties. The effect of the Tb^{3+} doping process on the luminescence performance and phase transition (cubic vs tetragonal) has been investigated by a joint use of experimental and first principle calculations on appropriate model systems. Moreover, this study enables us to construct a more consistent picture of the doping process of Tb^{3+} in ZrO_2 and provides a new approach for fabricating a multifunctional

Table 3
Coordinates (Xc, Yc), color purity, CCT and CRI of ZrO_2:x mol% Tb^{3+}.

Sample	Code	Xc, Yc	Color purity (%)	CCT (K)	CRI (%)	Color	LER (lm. W^{-1})
ZrO_2	I	(0.27, 0.34)	20.5	8730	76	Blue	279
ZrO_2: 1% Tb^{3+}	II	(0.31, 0.46)	33.7	5976	44	Yellowish Green	337
ZrO_2: 1% Tb^{3+}	III	(0.37, 0.54)	76.7	-	35	Yellow-green	386
ZrO_2: 4% Tb^{3+}	IV	(0.37, 0.55)	76.9	-	36	Green	507
ZrO_2: 8% Tb^{3+}	V	(0.38, 0.56)	80.5	-	31	Green	521

material and prospective application in lighting devices.

CRediT authorship contribution statement

Declaration of Competing Interest

None.

Acknowledgments

Supplementary materials

Supplementary material associated with this article can be found, in the online version, at doi:10.1016/j.materresbull.2021.111532.

References

[1] V. Balaram, Rare earth elements: a review of applications, occurrence, exploration, analysis, recycling, and environmental impact, Geosci. Front. 10 (2019) 1285.

[2] T. Cheisson, E.J. Schelter, Rare earth elements: Mendeleev's bane, modern marvels, Science 363 (2019) 489–493.

[3] M. Zhang, Z. X., M. Sun, T. Ma, Y. Huang, B. Huang, Y. Du, C. Yan, When rare earth meets carbon nanodots: mechanisms, applications and outlook, Chem. Soc. Rev. 49 (2020) 9220.

[4] N.O. Azarapin, A.S. Aleksandrovsky, V.V. Atuchin, T.A. Gavrilova, A.S. Krylov, M. S. Molokeev, S. Mukherjee, A.S. Oreshonkov, O.V. Andreev, Synthesis structural and spectroscopic properties of orthorhombic compounds baLnCuS$_3$ (Ln = Pr, Sm), J. Alloys Compd. 832 (2020), 153134.

[5] W. Li, J. Liu, D. Zhao, Mesoporous materials for energy conversion and storage devices, Nat. Rev. Mater. 1 (2016) 16023.

[6] K.L. Reddy, R. Balaji, A. Kumar, V. Krishnan, Lanthanide doped near infrared active upconversion nanophosphors: fundamental concepts, synthesis strategies, and technological applications, Small 14 (2018), 1801304.

[7] H. Xiong, Y. Zhang, Y. Liu, T. Gao, L. Zhang, Z.A Qiao, L. Zhang, S. Gan, Q. Huo, Self-template construction of honeycomb-like mesoporous YPO$_4$·Ln^{3+} (Ln = Eu, Tb) phosphors with tuneable luminescent properties, J. Alloys Compd. 782 (2019) 845–851.

[8] J.C.G. Bünzli, On the design of highly luminescent lanthanide complexes, Coord. Chem. Rev. 293 (2015) 19–47.

[9] S.N.C. Santos, K.T. Paula, J.M.P. Almeida, A.C. Hernandes, C.R. Mendonça, Effect of Tb^{3+}/Yb^{3+} in the nonlinear refractive spectrum of CaLiBO glasses, J. Non Cryst. Solids 524 (2019), 119637.

[10] T.O. Sales, R.J. Amjad, C. Jacinto, M.R. Dousti, Concentration dependent luminescence and crossrelaxation energy transfers in Tb^{3+} doped fluoroborate glasses, J. Lumin. 205 (2019) 282.

[11] V.X. Quang, P.V. Do, N.X. Ca, L.D. Thanh, V.P. Tuyen, P.M. Tan, V.X. Hoa, N. T. Hien, Role of modifier ion radius in luminescence enhancement from ^{5}D$_4$ level of Tb^{3+} ion doped alkali-alumino-telluroborate glasses, J. Lumin. 221 (2020), 117039.

[12] H. Guan, G. Liu, J. Wang, X. Dong, W. Yu, Multicolor tunable luminescence and paramagnetic properties of NaGdF$_4$:Tb^{3+}/Sm^{3+} multifunctional nanomaterials, Dalton Trans. 43 (2014) 10801–10808.

[13] P.V. Do, V.X. Quang, L.D. Thanh, V.P. Tuyen, N.X. Ca, V.X. Hoa, H.V. Tuyen, Energy transfer and white light emission of KGdF$_4$ polycrystalline co-doped with Tb^{3+}/Sm^{3+} ions, Opt. Mater. 92 (2019) 174–180.

[14] P.V. Do, N.X. Ca, L.D. Thanh, N.V. Nghia, T.T.C. Thuy, Optical properties and energy transfer in KYF$_4$.Sm^{3+} and KYF$_4$:Tb^{3+},Sm^{3+} polycrystalline materials, Phys. Chem. Chem. Phys. 22 (2020) 27590.

[15] V.P. Tuyen, V.X. Quang, N.M. Khaidukov, L.D. Thanh, N.X. Ca, N.V. Hao, N. V. Nghia, P.V. Do, K$_2$YF$_5$:Tb^{3+} single crystal: an in-depth study of spectroscopic properties, energy transfer and quantum cutting, Opt. Mater. 106 (2020), 109939.

[16] W.T. Carnall, P.R. Fields, K. Rajnak, Electronic energy levels in the trivalent lanthanide aquo ions. III. Tb^{3+}, J. Chem. Phys. 49 (1968) 4447.

[17] H. Guan, Y. Sheng, Y. Song, K. Zheng, C. Xu, X. Xie, Y. Dai, H. Zou, White light emitting, tunable color luminescence, energy transfer and paramagnetic properties of terbium and samarium doped BaGdF$_5$ multifunctional nanomaterials, RSC Adv. 6 (2016) 73160.

[18] F.H. Garzon, R. Mukundan, R. Lujan, E.L. Brosha, Solid state ionic devices for combustion gas sensing, Solid State Ion. 175 (2004) 487.

[19] L. Jin, Q. Yu, A. Rauf, C. Zhou, Elastic, electronic and thermal properties of YSZ from first principles, Solid State Sci. 14 (2012) 106.

[20] A.G. Sato, D.P. Volanti, D.M. Meira, S. Damyanova, E. Longo, J.M.C. Bueno, Effect of the ZrO$_2$ phase on the structure and behavior of supported Cu catalysts for ethanol conversion, J. Catal. 307 (2013) 1–17.

[21] F. Fleischhauer, R. Bermejo, R. Danzer, A. Mai, T. Graule, J. Kuebler, High temperature mechanical properties of zirconia tapes used for electrolyte supported solid oxide fuel cells, J. Power Sources 273 (2015) 237.

[22] L.X. Lovisa, V.D. Araujo, R.L. Tranquilin, E. Longo, M.S. Li, C.A. Paskocimas, M.R. D. Bomio, F.V. Motta, White photoluminescence emission from ZrO$_2$ co-doped with Eu^{3+}, Tb^{3+} and Tm^{3+}, J. Alloys Compd. 674 (2016) 245.

[23] S.S. Dj, T. Nenad B, V. Rastko, Photoluminescence properties of Er^{3+}/Yb^{3+} doped ZrO$_2$ coatings formed by plasma electrolytic oxidation, J. Lumin. 208 (2019) 296.

[24] L.X. Lovisa, J. Andrés, L. Gracia, M.Siu Li, C.A. Paskocimas, M.R.D. Bomio, V. D. Araújo, E. Longo, F.V. Motta, Photoluminescent properties of ZrO$_2$:Tm^{3+}, Tb^{3+}, Eu^{3+} powders-a combined experimental and theoretical study, J. Alloys Compd. 695 (2017) 3094.

[25] K. Joy, Optical and photoluminescence properties of nanostructured ZrO$_2$:Tb thin films, Thin Solid Films 556 (2019) 99.

[26] E. De La Rosa, L.A. Diaz-Torres, P. Salas, R.A. Rodríguez, Visible light emission under UV and IR excitation of rare earth doped ZrO$_2$ nanophosphor, Opt. Mater. 27 (2005) 1320.

[27] H. Zhang, Z. An, F. Li, Q. Tang, K. Lu, W. Li, Synthesis and characterization of mesoporous c-ZrO$_2$ microspheres consisting of peanut-like nano-grains, J. Alloys Compd. 454 (2008) 569.

[28] F. Gallino, C. Di Valentin, G. Pacchioni, Band gap engineering of bulk ZrO$_2$ by Ti doping, Phys. Chem. Chem. Phys. 13 (2011) 17667.

[29] K. Joy, V.M. L., Jijimon K. Thomas, P.V. Thomas, Effect of sol concentration on the structural, morphological, optical and photoluminescence properties of zirconia thin films, Thin Solid Films 520 (2012) 2683.

[30] M. Wang, J. Lin, X. Ning, X. Yang, X. Zhang, J. Zhao, Preparation and photoluminescence properties of Eu^{3+}-doped ZrO$_2$ nanotube arrays, Ceram. Int. 41 (2015) 8444.

[31] M. Wang, R. Xu, N. Fu, X. Wang, Preparation and photoluminescence properties of Tm^{3+}-doped ZrO$_2$ nanotube arrays, J. Alloys Compd. 674 (2016) 353.

[32] H. Singh, Sunaina, K.K. Yadav, V.K. Bajpai, M. Jha, Tuning the bandgap of m-ZrO$_2$ by incorporation of copper nanoparticles into visible region for the treatment of organic pollutants, Mater. Res. Bull. 123 (2020).

[33] A.B. Nawale, N.S. Kanhe, S.V. Bhoraskar, V.L. Mathe, A.K. Das, Influence of crystalline phase and defects in the ZrO$_2$ nanoparticles synthesized by thermal plasma route on its photocatalytic properties, Mater. Res. Bull. 47 (2012) 11.

[34] Y.L. Yang, X.L. Fan, C. Liu, R.X. Ran, First principles study of structural and electronic properties of cubic phase of ZrO$_2$ and HfO$_2$, Phys. B Condens. Matter 434 (2014) 7.

[35] Y. Zhang, H.X. Chen, L. Duan, J.B. Fan, L. Ni, V. Ji, A comparison study of the structural and mechanical properties of cubic, tetragonal, monoclinic, and three orthorhombic phases of ZrO$_2$, J. Alloys Compd. 749 (2018) 283–292.

[36] P. Li, I.W. Chen, J.E. Penner-Hahn, X-ray-absorption studies of zirconia polymorphs. I. Characteristic local structures, Phys. Rev. B Condens Matter 48 (1993) 10063.

[37] P. Li, I.W. Chen, J.E. Penner-Hahn, Effect of dopants on zirconia stabilization-An X-ray absorption study: I., Trivalent Dopants, J. Am. Ceram. Soc. 77 (1994) 118.

[38] C. Tiseanu, V. Parvulescu, D. Avram, B. Cojocaru, A.V. Vela-Gonzalez, M. Sanchez-Dominguez, Structural, down- and phase selective up-conversion emission properties of mixed valent Pr doped into oxides with tetravalent cations, Phys. Chem. Chem. Phys. 16 (2014) 5793.

[39] S.K. Gupta, V. Natarajan, Synthesis, characterization and photoluminescence spectroscopy of lanthanide ion doped oxide materials, BARC Newsl. 46 (2015) 14.

[40] C. Gionco, S. Hernández, M. Castellino, T.Ahmed Gadhi, J.A. Munoz-Tabares, E. Cerrato, A. Tagliaferro, N. Russo, M.C. Paganini, Synthesis and characterization of Ce and Er doped ZrO$_2$ nanoparticles as solar light driven photocatalysts, J. Alloys Compd. 775 (2019) 896.

[41] F. Goumrhar, L. Bahmad, O. Mounkachi, A. Benyoussef, Ferromagnetism in Mn and Fe doped ZrO_2 by ab-initio calculations, Comput. Condens. Matter 19 (2019) 00361.

[42] N. Tiwari, R.K. Kuraria, S.R. Kuraria, Effect of variable trivalent europium concentration on photo- and thermoluminescence of zirconium dioxide nanophosphors, Mater. Sci. Semicond. Process 31 (2015) 214.

[43] C. Colbea, D. Avram, B. Cojocaru, R. Negrea, C. Ghica, V.G. Kessler, G. A. Seisenbaeva, V.I. Parvulescu, C. Tiseanu, Full tetragonal phase stabilization in ZrO_2 nanoparticles using wet impregnation: Interplay of host structure, dopant concentration and sensitivity of characterization technique, Nanomaterials 8 (2018) 988.

[44] D. Liu, M. Wang, L. Gong, J. Zhao, M. Zhu, X. Wang, Photoluminescence properties of Eu^{3+} doped ZrO_2 with different morphologies and crystal structures, J. Alloys Compd. 864 (2021), 158781.

[45] Y.S. Vidya, H.Nagabhushana K.G., S.C. Sharma, K.S. Anantharaju, C. Shivakumara, D. Suresh, H.P. Nagaswarupa, S.C. Prashantha, M.R. Anilkumar, Phase transformation of $ZrO_2:Tb^{3+}$ nanophosphor: Color tunable photoluminescence and photocatalytic activities, J. Alloys Compd. 622 (2015) 86.

[46] Y. Hui, S. Zhao, J. Xu, L. Zhu, X. Zhou, B. Zou, Y. Wang, X. Cao, Doping concentration of Eu^{3+} as a fluorescence probe for phase transformation of zirconia, J. Rare Earths 33 (2015) 717.

[47] R. Marin, G. Sponchia, E. Zucchetta, P. Riello, F. Enrichi, G. De Portu, A. Benedetti, Monitoring the t → m martensitic phase transformation by photoluminescence emission in Eu^{3+}-doped zirconia powders, J. Am. Ceram. Soc. 96 (2013) 2628.

[48] I. Ahemen, F.B. Dejene, Effect of Eu^{3+} ion concentration on phase transition, site symmetry and quantum efficiency of ZrO_2 nanocrystal rods, J. Nanosci. Nanotechnol. 18 (2018) 2129.

[49] B. Marí, K.C. Singh, M. Sahal, S.P. Khatkar, V.B. Taxak, M. Kumar, Preparation and luminescence properties of Tb^{3+} doped ZrO_2 and $BaZrO_3$ phosphors, J. Lumin. 130 (2010) 2128.

[50] S. Das, C.Y. Yang, C.H. Lu, Structural and optical properties of tunable warm-white light-emitting $ZrO_2:Dy^{3+}$–Eu^{3+} nanocrystals, J. Am. Ceram. Soc. 96 (2013) 1602.

[51] S.D. Meetei, S.D. Singh, Hydrothermal synthesis and white light emission of cubic $ZrO_2:Eu^{3+}$ nanocrystals, J. Alloys Compd. 587 (2014) 143.

[52] B. Toby, EXPGUI, a graphical user interface for GSAS, J. Appl. Crystallogr. 34 (2001) 210–213.

[53] H. Rietveld, A profile refinement method for nuclear and magnetic structures, J. Appl. Crystallogr. 2 (1969) 65–71.

[54] J.P. Perdew, M. Ernzerhof, K. Burke, Rationale for mixing exact exchange with density functional approximations, J. Chem. Phys. 105 (1996) 9982.

[55] S. Grimme, A. J., S. Ehrlich, H. Krieg, A consistent and accurate ab initio parametrization of density functional dispersion correction (DFT-D) for the 94 elements H-Pu, J. Chem. Phys. 132 (2010), 154104.

[56] S.N Basahel, T.T. Al, M. Mokhtar, K. Narasimharao, Influence of crystal structure of nanosized ZrO_2 on photocatalytic degradation of methyl orange, Nanoscale Res. Lett. 10 (2015) 73.

[57] V. Shukla, K. Balani, A. Subramaniam, S. Omar, Effect of thermal aging on the phase stability of $1Yb_2O_3$–xSc_2O_3– (99 −<x)ZrO_2 (x = 7, 8 mol %), J. Phys. Chem. C 123 (2019) 21982.

[58] S. Vasanthavel, S. Kannan, Structural investigations on the tetragonal to cubic phase transformations in zirconia induced by progressive yttrium additions, J. Phys. Chem. Solids 112 (2018) 100–105.

[59] B. Peng, K. Song, S. Zhang, S. Shen, J. Xu, J. Wu, W. Su, Color-tunable light emission of $SrLa_{4-x-y}Si_3O_{13}:xTb^{3+}$, yEu^{3+} phosphors by energy transfer process for warm white LEDs, AIP Adv. 8 (2018), 015119.

[60] N.N. Sarkar, K.G. Rewatkar, V.M. Nanoti, N.T. Tayade, D.S. Bhowmick, Structural and magnetic study of Zr^{4+} substituted magnesium ferrite nano-particles, J. Phys. Sci. 22 (2017) 107.

[61] M.J. McKelvy, R. Sharma, A.V.G. Chizmeshya, R.W. Carpenter, K. Streib, Magnesium hydroxide dehydroxylation: in situ nanoscale observations of lamellar nucleation and growth, Chem. Mater. 13 (2001) 921.

[62] F.V. Motta, A.P.A. Marques, M.S. Li, M.F.C. Abreu, C.A. Paskocimas, M.R.D. Bomio, R.P. Souza, J.A. Varela, E. Longo, Preparation and photoluminescence characteristics of $In(OH)_3:xTb^{3+}$ obtained by Microwave-Assisted Hydrothermal method, J. Alloys Compd. 533 (2013) 338.

[63] A. Kumar, A. Jaiswal, M. Sanbui, S. Omar, Oxygen-ion conduction in scandia-stabilized zirconia-ceria solid electrolyte (xSc_2O_3–$1CeO_2$–(99–x)ZrO_2, 5 ≤ x ≤ 11), J. Am. Ceram. Soc. 100 (2017) 659–668.

[64] A. Kumar, A. Jaiswal, M. Sanbui, S. Omar, Scandia stabilized zirconia-ceria solid electrolyte ($xSc1CeSZ$, 5 < x < 11) for IT-SOFCs: structure and conductivity studies, Scr. Mater. 121 (2016) 10–13.

[65] C.G. Kontoyannis, M. Orkoula, Quantitative determination of the cubic, tetragonal and monoclinic phases in partially stabilized zirconias by Raman spectroscopy, J. Mater. Sci. 29 (1994) 5316.

[66] P. Bouvier, H.C. Gupta, G. Lucazeau, Zone center phonon frequencies in tetragonal zirconia: lattice dynamical study and new assignment proposition, J. Phys. Chem. Solids 62 (2001) 873–879.

[67] C. Tiseanu, V.I. Parvulescu, B. Cojocaru, K. Pemartin, M. Sanchez-Dominguez, M. Boutonnet, In situ Raman and time-resolved luminescence investigation of the local structure of ZrO_2 in the amorphous to crystalline phase transition, J. Phys. Chem. C 116 (2012) 16776.

[68] C.N. Chervin, B.J. Clapsaddle, H.W. Chiu, A.E. Gash, J.H. Satcher Jr, S. M. Kauzlarich, Aerogel synthesis of yttria-stabilized zirconia by a non-alkoxide sol-gel route, Chem. Mater. 17 (2005) 3345–3351.

[69] S. Vasanthavel, B. Derby, S. Kannan, Tetragonal to cubic transformation of SiO_2 stabilized ZrO_2 polymorph through dysprosium substitutions, Inorg. Chem. 56 (2017) 1273–1281.

[70] H. Fujimori, M. Yashima, M. Kakihana, M. Yoshimura, Structural changes of scandia-doped zirconia solid solutions: rietveld analysis and Raman scattering, J. Am. Ceram. Soc. 81 (1998) 2885.

[71] M. Yashima, K. Ohtake, M. Kakihana, H. Arashi, M. Yoshimura, Determination of tetragonal-cubic phase boundary of $Zr_{1−x}R_xO_{2−x/2}$ (R= Nd, Sm, Y, Er and Yb) By Raman scattering, J. Phys. Chem. Solids 57 (1996) 17.

[72] G. Jomard, T. Petit, A. Pasturel, L. Magaud, G. Kresse, J. Hafner, First-principles calculations to describe zirconia pseudopolymorphs, Phys. Rev. B 59 (1999) 4044.

[73] Y. Wang, C. Cai, L. Li, L. Yang, Y. Zhou, G. Zhou, Oxygen vacancy ordering induced displacements of cations in yttria-stabilized zirconia, AIP Adv. 6 (2016), 095113.

[74] P. Kubelka, K. Munk, Ein beitrag zur optik der farbanstriche, Z. Für Tech. Phys. 12 (1931) 593.

[75] V. Kumar, V.Kumar S.Som, V. Kumar, O.M. Ntweaborwa, E. Coetsee, H.C. Swart, Tunable and white emission from $ZnO:Tb^{3+}$ nanophosphors for solid state lighting applications, Chem. Eng. J. 255 (2014) M541.

[76] R. Nedzinskas, B. Čechavičius, V. Karpus, J. Kavaliauskas, G. Valušis, L.H. Li, S. P. Khanna, E.H. Linfield, Photoreflectance and photoluminescence studies of epitaxial InGaAs quantum rods grown with As_2 and As_4 sources, J. Appl. Phys. 109 (2011), 123526.

[77] E. Longo, D.P. Volanti, V.M. Longo, I.C.Nogueira L.G.racia, M.A.P. Almeida, A. N. Pinheiro, M.M. Ferrer, L.S. Cavalcante, J. Andreś, Toward an understanding of the growth of Ag filaments on α-Ag_2WO_4 and their photoluminescent properties: a combined experimental and theoretical study, J. Phys. Chem. C 118 (2014) 1229.

[78] K. Hachiya, H. Oku, J. Kondoh, Photoluminescence in yttria-stabilized zirconia of aging effects, Phys. Rev. B 71 (2005), 064111.

[79] V.M. Longo, L.S. Cavalcante, A.T. de Figueiredo, L.P.S. Santos, et al., Highly intense violet-blue light emission at room temperature in structurally disordered $SrZrO_3$ powders, Appl. Phys. Lett. 90 (2007), 091906.

[80] V.M. Longo, L.S. Cavalcante, R. Erlo, V.R. Mastelaro, et al., Strong violet–blue light photoluminescence emission at room temperature in $SrZrO_3$: joint experimental and theoretical study, Acta Mater. 56 (2008) 2191.

[81] K. Smits, L. Grigorjeva, D. Millers, A. Sarakovskis, J. Grabis, W. Lojkowski, Intrinsic defect related luminescence in ZrO_2, J. Lumin. 131 (2011) 2058.

[82] M. Boffelli, W. Zhu, M. Back, G. Sponchia, T. Francese, P. Riello, A. Benedetti, G. Pezzotti, Oxygen hole states in zirconia lattices: quantitative aspects of their cathodoluminescence emission, Phys. Chem. A 118 (2014) 9828.

[83] R. Martínez-Martínez, G. Juárez-López, M. García-Hipólito, J.J. Bautista Díaz, S. C. Téllez, M.A. Aguilar-Frutis, G.A. Flores, C. Falcony, Blue and bluish-white colors from the luminescent ZrO_2 and ZrO_2: Al^{3+} films prepared by the USP method, Mater. Res. Express 8 (2021), 016201.

[84] P.F.S. Pereira, C.C.S., A.F. Gouveia, M.M. Ferrer, I.M. Pinatti, G. Botelho, J. R. Sambrano, I.L.V. Rosa, J. Andres, E. Longo, α-$Ag_{2−2x}Zn_xWO_4$ (0 ≤ x ≤ 0.25) Solid solutions: structure, morphology, and optical properties, Inorg. Chem. 56 (2017) 7360.

[85] N.G. Petrik, D.P. Taylor, T.M. Orlando, Laser-stimulated luminescence of yttrias-tabilized cubic zirconia crystals, J. Appl. Phys. 85 (1999) 6770.

[86] R. Devanathan, W.J. Weber, S.C. Singhal, J.D. Gale, Computer simulation of defects and oxygen transport in yttrias-tabilized zircônia, Solid State Ion. 177 (2006) 1251.

[87] S. Lis, Factors affecting Luminescence intensity of lanthanide ions analytical apllications of lanthanide luminescence in solution, Acta Phys. Polon. A 84 (1993) 1003.

[88] J.C.G. Bunzli, G.R. Choppin, Lanthanide Probes in Life, Chemical and Earths Sciences, Elsevier, Amsterdam, 1989. Chap. 7.

[89] G. Blasse, Energy transfer between inequivalent Eu^{2+} ions, J. Solid State Chem. 62 (1986) 207.

[90] F. Kang, Y. Zhang, M. Peng, Controlling the energy transfer via multi luminescent centers to achieve white light/tunable emissions in a single-phased X2-type Y_2SiO_5: Eu^{3+},Bi^{3+} phosphor for ultraviolet converted LEDs, Inorg. Chem. 54 (2015) 1462.

[91] Y.F. Wu, Y.T. Nien, Y.J. Wang, I.G. Chen, Enhancement of photoluminescence and color purity of $CaTiO_3:Eu$ phosphor by Li doping, J. Am. Ceram. Soc. 95 (2012) 1360.